

# Simultaneous Searching of Globally Optimal Interacting Surfaces with Shape Priors

Qi Song

Xiaodong Wu

Yunlong Liu

Mona Garvin

Milan Sonka

Department of Electrical and Computer Engineering

The University of Iowa, Iowa City, IA 52242, USA

qi-song, xiaodong-wu, yunlong-liu, mona-garvin, milan-sonka@uiowa.edu

## Abstract

*Multiple surface searching with only image intensity information is a difficult job in the presence of high noise and weak edges. We present in this paper a novel method for globally optimal multi-surface searching with a shape prior represented by convex pairwise energies. A 3-D graph-theoretic framework is employed. An arc-weighted graph is constructed based on a shape model built from training datasets. A wide spectrum of constraints is then incorporated. The shape prior term penalizes the local topological change from the original shape model. The globally optimal solution for multiple surfaces can be obtained by computing a maximum flow in low-order polynomial time. Compared with other graph-based methods, our approach provides more local and flexible control of the shape. We also prove that our algorithm can handle the detection of multiple crossing surfaces with no shared voxels. Our method was applied to several application problems, including medical image segmentation, scenic image segmentation, and image resizing. Compared with results without using shape prior information, our improvement was quite impressive, demonstrating the promise of our method.*

## 1. Introduction

Recently, graph based methods with a global energy optimization property have attracted considerable attention in computer vision [2, 3, 9, 6]. Despite their wide applicability for image segmentation, the graph based methods often perform poorly in the presence of weak image edges, high noise or object occlusions [18]. The incorporation of shape prior information is important to prevent such failures.

Currently, many attempts have been made to incorporate shape prior information. Felzenszwalb [7] used triangulated polygons to represent and detect deformable shapes in images. Schoenemann *et al.* [16] employed a ratio functional

to incorporate the elastic shape priors. Both methods only work for single surface detection in 2-D cases. Several algorithms were proposed based on the graph-cut framework, which has become very popular in the computer vision and graphics fields in recent years. Freedman *et al.* [8] devised an interactive shape prior segmentation method based on graph cut algorithms. The graph edge-weights were employed, which contained information about a level-set function of a shape template. Malcolm *et al.* [15] incorporated the prior shape information from kernel PCA into an iterative graph cut framework. Vu *et al.* [18] presented a multiple object segmentation framework. The shape energy based on a shape distance function is incorporated via the weights of the edges connected with the terminals.

In this paper, we propose a new method for simultaneous searching of globally optimal interacting surfaces with shape priors in 3-D, which is mainly based on the graph searching framework proposed by Wu *et al.* [19] and Li *et al.* [14]. The basic idea is presented, as follows. A shape model is first built for each target object based on the prior information from the training datasets, which reflects the approximate topological structure information of the target surfaces. The graph is then constructed based on this shape model. Multiple constraints are incorporated into the graph, e.g., the surface monotonicity constraint, the hard shape constraint, the surface interaction constraint, as well as other prior knowledge elements. A shape prior term using convex pairwise energies is added to our energy function, which can be incorporated into the graph by utilizing specific graph arc weights. The optimal solution is computed by solving a maximum flow problem. In our framework, the sought surfaces are allowed to pass through the same voxel (Fig. 1(a)). However, in some applications, e.g., the image resizing problem, multiple height-field surfaces (seams) in the image need to be removed or inserted to change the image size. Those surfaces may cross each other, but cannot pass through the same pixel (the same pixel can-

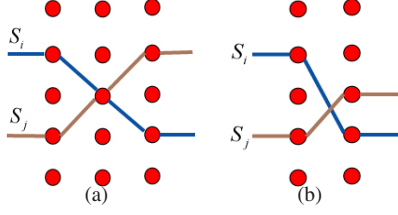


Figure 1. (a) Two surfaces cross at a specific voxel. (b) No two crossing surfaces pass through the same voxel.

not be removed twice), as shown in Fig. 1(b). In this paper, we prove that when applying the same cost function and shape prior function to all surfaces, the problem of finding multiple crossing surfaces without passing through the same voxel can be transformed into a problem of finding an optimal solution of multiple non-crossing surfaces, which can be solved in our framework by adding proper surface interacting constraints.

The major difference between our method and the graph-cut based methods when considering the shape priors is that our graph is constructed on a specific preferred shape model, which allows easy incorporation of a wide spectrum of shape prior information. Compared with graph-cut based methods, our framework provides a more local and flexible control. In addition, incorporating simultaneous detection of “mutually” interacting surfaces into the graph-cut framework is non-trivial. Delong and Boykov’s work [5] is one step towards that goal.

Ishikawa [12] developed a method for the multi-labeled MRF optimization with convex priors, which is closely related to our work. While interpreting a configuration of the multi-labeled MRF model as a surface in the corresponding (geometric) graph, Ishikawa’s method can be used to detect only a single optimal surface. In this work, we strive to simultaneously compute multiple mutually interacting optimal configurations (surfaces) with additional geometric constraints, which finds important applications in medical image segmentation and others. Li *et al.* [13] have developed a framework based on a graph searching approach with elliptic shape model priors. His method was only applicable to multiple surface detection of a *single* object. Recently, Song *et al.* incorporated linear soft smoothness penalty in a method for simultaneous segmentation of human pelvic structures [17]. The linear function limited the flexibility of the constraints. Besides, none of these methods have the capability of handling the problem with the requirement that no two target surfaces can pass through the same voxel.

To assess the power of our approach, our new method was tested in several diverse applications. The experiments show that our approach produces highly accurate results.

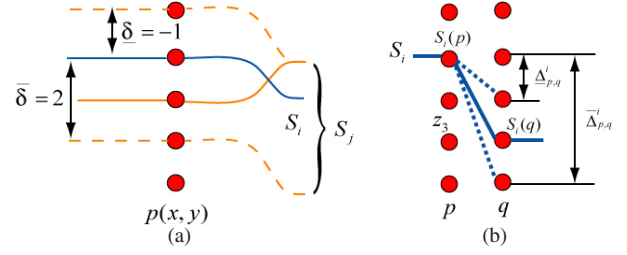


Figure 2. (a) Surface interacting constraints. The blue solid line represents  $S_i$ . Dashed lines show the possible range of  $S_j$ . One example of  $S_j$  is represented by the yellow solid line. (b) Hard shape constraints between columns  $p$  and  $q$  on surface  $S_i$ .

## 2. Methods

We start from a shape model obtained from the training datasets for each sought surface, which contains the basic topological structure information for the sought surface. A mesh is then constructed from this shape model. Note that trivial surface geometries (e.g., terrain-like surfaces) may not need a shape model and allow a direct definition of the mesh [14]. The input image is resampled along a ray intersecting every vertex of the mesh (one ray per mesh vertex). A vector of voxels is created from resampling, which is expected to contain one voxel on the sought surface. Following these two steps, a new volumetric image is formed from these voxel vectors. Our task is to search for terrain-like surfaces simultaneously in the new volumetric image.

### 2.1. Problem Formulation

Let  $\mathcal{I}(X, Y, Z)$  of size  $X \times Y \times Z$  be a given 3-D volumetric image. For each  $(x, y)$  pair, the voxel subset  $\{\mathcal{I}(x, y, z) | 0 \leq z < Z\}$  forms a column parallel to the  $z$ -axis, denoted by  $p(x, y)$ . Each column has a set of neighbors for a certain neighbor setting  $\mathcal{N}$ , e.g., four-neighbor relationship [14]. The problem is to find  $\lambda$  terrain-like surfaces which intersect each column  $p(x, y)$  at exactly one voxel. Thus, the terrain-like surface  $S_i$  can be defined as a function  $S_i(x, y)$ , mapping  $(x, y)$  pairs to their  $z$ -values. An edge-based cost  $c_i(x, y, z)$  is assigned to each voxel  $\mathcal{I}(x, y, z)$  for surface  $S_i$ , which is inversely related to the likelihood that the desired surface  $S_i$  contains the voxel.

A surface interacting constraint is added to the column  $p(x, y)$  for each pair of the sought surfaces  $S_i$  and  $S_j$ . For each  $p(x, y)$ , we have  $\bar{\delta} \leq S_i(p) - S_j(p) \leq \bar{\delta}$ , where  $\bar{\delta}$  and  $\bar{\delta}$  are two specified surface interacting parameters for  $S_i$  and  $S_j$  (Fig. 2(a)). Note that if  $\bar{\delta} \cdot \bar{\delta} \leq 0$ , two surfaces may cross each other at the same voxel. However, in some applications (e.g., the image resizing problem), two surfaces may cross each other but cannot pass through the same voxel. Thus, in those applications we also required that two interacting surfaces can not pass through the same voxel.

To incorporate the shape information, two kinds of shape constraints are enforced: the hard shape constraint and the shape-prior penalties. Specifically, for any pair of neighboring columns  $p$  and  $q$ , the hard shape constraint is defined as follows:  $\underline{\Delta}_{p,q}^i \leq S_i(p) - S_i(q) \leq \overline{\Delta}_{p,q}^i$ , where  $\underline{\Delta}_{p,q}^i$  and  $\overline{\Delta}_{p,q}^i$  are shape the constraint parameters between  $p$  and  $q$  for  $S_i$  (Fig. 2(b)). The shape-prior penalties can be expressed as  $f_{p,q}^i(S_i(p) - S_i(q))$ , where  $f_{p,q}^i$  is a convex function penalizing the shape changes of  $S_i$  on  $p$  and  $q$ .

The overall energy of the set  $\mathcal{S}$  of  $\lambda$  surfaces  $S_i$ 's takes the form:

$$E(\mathcal{S}) = \sum_{i=1}^{\lambda} \sum_{I_i(x,y,z) \in S_i} c_i(x,y,z) + \sum_{i=1}^{\lambda} \sum_{(p,q) \in \mathcal{N}} f_{p,q}^i(S_i(p) - S_i(q)). \quad (1)$$

Our goal is to find an optimal set of  $\lambda$  surfaces such that (a) each pair of surfaces satisfies the surface interacting constraint; (b) each surface satisfies the hard shape constraint; and (c) the energy (1) is minimized. For some applications, we also require that no two interacting surfaces pass through a same voxel.

## 2.2. Algorithms

Our algorithms are mainly based on the graph-search framework [14]. An arc-weighted graph representation is employed to incorporate the surface interacting constraint and the shape constraints. The optimal solution to the energy minimization problem in (1) can be achieved by solving a maximum flow problem. In Section 2.2.1 we give the details of our arc-weighted graph search method. For the detection of multiple surfaces that may cross each other and share no common voxels, we prove in Section 2.2.2 that if we use the same cost functions and shape prior constraints for all target surfaces, there exists an optimal solution consisting of non-crossing surfaces with the minimum distance between any two adjacent surfaces no less than 1.

### 2.2.1 Arc-Weighted Graph Search

The basic idea for solving the arc-weighted graph search problem is to reduce it into a maximum flow problem. A directed graph  $G$  containing  $\lambda$  node-disjoint subgraphs  $\{G_i = (V_i, E_i) : i = 1, 2, \dots, \lambda\}$  is defined, in which every node  $V_i(x, y, z) \in V_i$  represents exactly one voxel  $\mathcal{I}(x, y, z)$ .

To enforce a variety of geometric constraints, the following arcs are constructed.

**Intra-column arcs:** To ensure the monotonicity of the target surfaces (i.e., the target surface intersects with each

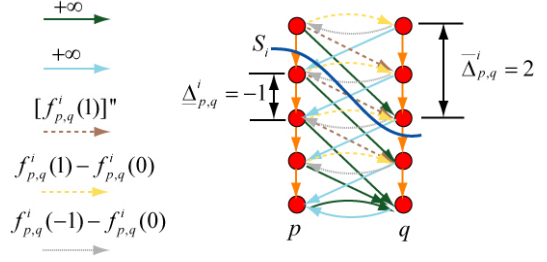


Figure 3. Graph construction for the convex shape prior function. Green and blue arcs of weight  $+\infty$  reflect the hard shape constraints. Weighted arcs brown, yellow and gray are built for shape prior penalties. Here we suppose  $[f_{p,q}^i(0)]' = 0$ .  $S_i$  cuts the arcs with a total weight of  $f_{p,q}^i(2)$ .

column exactly once), intra-column arcs are added. Along every column  $p(x, y)$ , each node  $V_i(x, y, z)$  has a directed edge with  $+\infty$  weight to the node immediately below it (i.e.,  $V_i(x, y, z - 1)$ ).

**Inter-surface arcs:** To enforce the surface interacting constraints  $\underline{\delta} \leq S_i(x, y) - S_j(x, y) \leq \bar{\delta}$  between any two sought surfaces  $S_i$  and  $S_j$ , the inter-surface arcs are added. For each  $p(x, y)$ , a directed arc with  $+\infty$  weight is added from each node  $V_i(x, y, z)$  to  $V_j(x_1, y_1, z - \bar{\delta})$  to make sure that  $S_i(x, y) - S_j(x, y) \leq \bar{\delta}$ . On the other hand, each node  $V_j(x, y, z)$  also has a directed arc with  $+\infty$  to  $V_i(x, y, z + \underline{\delta})$  such that  $\underline{\delta} \leq S_i(x, y) - S_j(x, y)$ .

**Inter-column arcs:** The remaining problem is how to incorporate the shape constraints in our graph construction. To add the hard shape constraints, the inter-column arcs are added as follows. Let  $p(x_1, y_1)$  and  $q(x_2, y_2)$  be two neighboring columns. The hard shape constraint has the following form:  $\underline{\Delta}_{p,q}^i \leq S_i(p) - S_i(q) \leq \overline{\Delta}_{p,q}^i$ . A directed arc with  $+\infty$  weight is put from each node  $V_i(x_1, y_1, z)$  to the node  $V_i(x_2, y_2, z - \overline{\Delta}_{p,q}^i)$ . Meanwhile, we have a directed arc with  $+\infty$  weight from the node  $V_i(x_2, y_2, z)$  to  $V_i(x_1, y_1, z + \underline{\Delta}_{p,q}^i)$ .

To incorporate the shape prior penalty, additional inter-column arcs are employed. To “distribute” the convex shape prior penalty  $f_{p,q}^i(S_i(p) - S_i(q))$  to the corresponding cuts between the columns in  $G$ , we make use of the (discrete equivalent of) second derivative of  $f_{p,q}^i(\cdot)$ ,  $[f_{p,q}^i(h)]'' = [f_{p,q}^i(h+1) - f_{p,q}^i(h)] - [f_{p,q}^i(h) - f_{p,q}^i(h-1)]$ . Since  $f_{p,q}^i(h)$  is a convex function,  $[f_{p,q}^i(h)]'' \geq 0$ . For each  $h = \underline{\Delta}_{p,q}^i + 1, \underline{\Delta}_{p,q}^i + 2, \dots, \overline{\Delta}_{p,q}^i - 1$ , if  $[f_{p,q}^i(h)]' \geq 0$ , an arc from  $V_i(x_1, y_1, z)$  to  $V_i(x_2, y_2, z - h)$  carries an arc-weight of  $[f_{p,q}^i(h)]''$ . If  $[f_{p,q}^i(h)]' \leq 0$ , an arc from  $V_i(x_2, y_2, z)$  to  $V_i(x_1, y_1, z + h)$  has the weight of  $[f_{p,q}^i(h)]''$ , as shown in Fig. 3. Note that if  $h = h_0^+ = \min\{h | [f_{p,q}^i(h)]' \geq 0\}$ , we let  $[f_{p,q}^i(h_0^+)]'' = f_{p,q}^i(h_0^+ + 1) - f_{p,q}^i(h_0^+)$  for arcs from  $V_i(x_1, y_1, z)$  to  $V_i(x_2, y_2, z - h_0^+)$ . If  $h =$

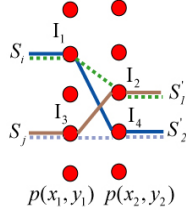


Figure 4. Surface transform from the crossing surfaces (blue and brown) into non-crossing surfaces (green and gray).

$h_0^- = \max\{h | [f_{p,q}^i(h)]' \leq 0\}$ , we let  $[f_{p,q}^i(h_0^-)]'' = f_{p,q}^i(h_0^- - 1) - f_{p,q}^i(h_0^-)$  for arcs from  $V_i(x_2, y_2, z)$  to  $V_i(x_1, y_1, z + h_0^-)$ .

In the following, we show that using this construction, the total weight of the arcs that are cut by  $S_i$  between two neighboring columns  $p$  and  $q$  equals to the shape prior penalty  $f_{p,q}^i(S_i(p) - S_i(q))$ .

Let  $S_i(p) - S_i(q) = d$ , where  $\underline{\Delta}_{p,q}^i \leq d \leq \bar{\Delta}_{p,q}^i$ . WLOG, we assume that  $f_{p,q}^i(h_0^+) = 0$  (otherwise we can subtract  $f_{p,q}^i(h_0^+)$  from the weight of each arc from  $p$  to  $q$  without essentially affecting the total arc-weights). Similarly, we can assume that  $f_{p,q}^i(h_0^-) = 0$ . According to our arc construction, if  $[f_{p,q}^i(d)]' > 0$ , then  $S_i$  cuts the arcs with a total weight of  $\sum_{j=1}^{d-h_0^+} j[f_{p,q}^i(d-j)]'' = f_{p,q}^i(d) - f_{p,q}^i(h_0^+) = f_{p,q}^i(d)$ . If  $[f_{p,q}^i(d)]' < 0$ , then  $S_i$  cuts the arcs with a total weight of  $\sum_{j=1}^{h_0^- - d} j[f_{p,q}^i(d+j)]'' = f_{p,q}^i(d) - f_{p,q}^i(h_0^-) = f_{p,q}^i(d)$ . If  $[f_{p,q}^i(d)]' = 0$ , no arc is cut, the total weight is 0. Thus, the total weight of the arcs that are cut by  $S_i$  between neighboring columns  $p$  and  $q$  equals to the shape prior penalty  $f_{p,q}^i(S_i(p) - S_i(q))$  [19], which penalizes the shape change of the surface  $S_i$  between the two columns.

With this constructed graph  $G$ , we can find an optimal cut  $\mathcal{C}^* = (A^*, \bar{A}^*)$  ( $A^* \cup \bar{A}^* = V$ ) in  $G$ , minimizing the total weight of nodes in  $A^*$  and the total arc weight of  $\mathcal{C}^*$ . The optimal cut corresponds to the optimal set of  $\lambda$  surfaces in  $\mathcal{I}$ , which minimizes our energy  $E(\mathcal{S})$ . As described in [19], this optimal cut can be found by solving a maximum flow problem in a low-order polynomial time.

### 2.2.2 Detecting Multiple Surfaces with No Common Voxels

In this section, we consider the multiple surface detection problem, in which no two surfaces share a common voxel. Note that in this surface detection problem, no surface interacting constraint is enforced. We prove that if using the same cost functions and shape prior constraints for all sought surfaces, an optimal solution to this problem exists, which consists of non-crossing surfaces with minimum distance of 1 between any two adjacent ones.

Let  $\mathcal{S} = \{S_1, S_2, \dots, S_\lambda\}$  denote the optimal set of  $\lambda$  sought surfaces.  $\mathcal{V}$  represents the union of all voxels on those surfaces. Let  $S'_1(p)$  denote the maximum z-coordinate of the voxels in  $\mathcal{V}$  on each column  $p(x, y)$ . This results in a new surface  $S'_1$  in  $\mathcal{I}$ . Remove all voxels on  $S'_1$  from  $\mathcal{V}$ . Then let  $S'_2(p)$  denote the maximum z-coordinate of the voxels in  $\mathcal{V} - S'_1$ . This results in another new surface  $S'_2$ . By doing this iteratively, we can obtain a new set of  $\lambda$  surfaces, denoted as  $\mathcal{S}' = \{S'_1, S'_2, \dots, S'_\lambda\}$ . In the following, we prove that  $\mathcal{S}'$  is an optimal solution.

First, from the construction of the  $\mathcal{S}'$ , each surface  $S'_i$  intersects each column  $p(x, y)$  at exactly one voxel. We next prove by induction that  $\mathcal{S}'$  satisfies the hard shape constraint and the total shape-prior penalty on  $\mathcal{S}'$  are no larger than that on  $\mathcal{S}$ .

Consider two neighboring voxels  $I_1 = \mathcal{I}(x_1, y_1, z_1)$  and  $I_2 = \mathcal{I}(x_2, y_2, z_2)$  on  $S'_1$ . If they both belong to the same surface  $S$ , they satisfy the hard shape constraint and the shape prior penalty on the arc  $(I_1, I_2)$  does not change. Otherwise, suppose  $I_1 \in S_i$  and  $I_2 \in S_j$  ( $i \neq j$ ). Let  $I_3 = \mathcal{I}(x_1, y_1, z_3)$  denote the voxel on  $S_j$ , which intersects with  $p(x_1, y_1)$ , and  $I_4 = \mathcal{I}(x_2, y_2, z_4)$  denote the voxel on  $S_i$ , which intersects with  $p(x_2, y_2)$  (Fig. 4). Since  $S'_1(x, y)$  is the maximum z-coordinate of the voxels in  $\mathcal{V}$  on each column  $p(x, y)$ , we have  $z_1 > z_3 \geq 0$  and  $z_2 > z_4 \geq 0$ . Note that  $S_i$  and  $S_j$  are feasible surfaces. Thus  $\underline{\Delta}_{1,2} \leq z_1 - z_4 \leq \bar{\Delta}_{1,2}$  and  $\underline{\Delta}_{1,2} \leq z_3 - z_2 \leq \bar{\Delta}_{1,2}$ , where  $\underline{\Delta}_{1,2}$  and  $\bar{\Delta}_{1,2}$  are specified shape constraint parameters between  $p(x_1, y_1)$  and  $p(x_2, y_2)$  for sought surfaces. Therefore,  $\underline{\Delta}_{1,2} \leq z_1 - z_2 \leq \bar{\Delta}_{1,2}$ , which indicates that  $S'_1$  satisfies the hard shape constraint. In the meanwhile, we have  $\underline{\Delta}_{1,2} \leq z_3 - z_4 \leq \bar{\Delta}_{1,2}$ . Thus,  $\mathcal{V} - S'_1$  forms a set  $\mathcal{S}_{\lambda-1}$  of  $\lambda - 1$  feasible surfaces. We next look into the change of the total shape prior penalty. From the computation of  $S'_1$ , we replace the old arcs  $(I_1, I_4)$  and  $(I_3, I_2)$  by two new arcs  $(I_1, I_2)$  and  $(I_3, I_4)$  to obtain  $S'_1$  and  $\mathcal{S}_{\lambda-1}$ . The total shape prior penalty on the new arcs  $(I_1, I_2)$  and  $(I_3, I_4)$  is  $f(z_1 - z_2) + f(z_3 - z_4)$  and that on the old arcs  $(I_1, I_4)$  and  $(I_3, I_2)$  is  $f(z_1 - z_4) + f(z_3 - z_2)$ . Since  $z_1 > z_3$  and  $z_2 > z_4$ , we have  $z_1 - z_2 < z_1 - z_4$ ,  $z_1 - z_2 > z_3 - z_2$ ,  $z_3 - z_4 < z_1 - z_4$  and  $z_3 - z_4 > z_3 - z_2$ . Due to the convexity of the function  $f$ , we have  $f(z_3 - z_4) \leq \{(z_1 - z_3)/(z_1 + z_2 - z_3 - z_4)\}f(z_3 - z_2) + \{(z_2 - z_4)/(z_1 + z_2 - z_3 - z_4)\}f(z_1 - z_4)$  and  $f(z_1 - z_2) \leq \{(z_2 - z_4)/(z_1 + z_2 - z_3 - z_4)\}f(z_3 - z_2) + \{(z_1 - z_3)/(z_1 + z_2 - z_3 - z_4)\}f(z_1 - z_4)$ . Adding them together, we got

$$f(z_1 - z_2) + f(z_3 - z_4) \leq f(z_1 - z_4) + f(z_3 - z_2).$$

Hence, the total shape prior penalty of the resulting  $\lambda$  surfaces (i.e.,  $S'_1$  and  $\lambda - 1$  surfaces in  $\mathcal{S}_{\lambda-1}$ ) is no larger than that of  $\mathcal{S}$ .

Let  $\mathcal{S}_{\lambda-l}$  denote the remaining  $\lambda - l$  surfaces in the so-



lution after we compute the first  $l$  surfaces  $S'_1, S'_2, \dots, S'_l$ . Assume that all those  $l$  surfaces satisfy the hard shape constraint, and the total shape prior penalty of those  $l$  surfaces and the  $\lambda - l$  surfaces in  $\mathcal{S}_{\lambda-l}$  does not increase comparing to that of  $\mathcal{S}$ . We need to prove that after computing the  $(l + 1)$ st surface  $S'_{l+1}$ , the non-increasing property of the total shape prior penalty is still hold and  $S'_{l+1}$  satisfy the hard shape constraint. Notice that  $S'_{l+1}$  is computed from the vertex set  $\mathcal{V} - \cup_{k=1}^l S'_k$ , which forms the feasible  $\lambda - l$  surfaces in  $\mathcal{S}_{\lambda-l}$ . We can use exactly the same argument as we do for  $S'_1$ , which shows that  $S'_{l+1}$  satisfies the hard shape constraint and the non-increasing property of the total shape prior penalty is hold. We thus prove that  $\mathcal{S}'$  is a feasible solution and the total shape prior penalty of  $\mathcal{S}'$  is no larger than that of  $\mathcal{S}$ .

Since  $\mathcal{S}$  is an optimal solution, no two surfaces in  $\mathcal{S}$  pass through the same voxel. It is obvious that no common voxels may present in any two surfaces in  $\mathcal{S}'$ . The union of the voxels on the surfaces in  $\mathcal{S}$  is the same as the union of the voxels on the surfaces in  $\mathcal{S}'$ . Thus,  $\sum_{i=1}^{\lambda} \sum_{I_i(x,y,z) \in \mathcal{S}_i} c_i(x,y,z) = \sum_{i=1}^{\lambda} \sum_{I_i(x,y,z) \in \mathcal{S}'_i} c_i(x,y,z)$ .

Hence, the total energy  $E(\mathcal{S}')$  of the  $\lambda$  surfaces in  $\mathcal{S}'$  is no larger than that of  $\mathcal{S}$ , that is,  $E(\mathcal{S}') \leq E(\mathcal{S})$ . Since  $\mathcal{S}$  is an optimal set of surfaces,  $\mathcal{S}'$  is an optimal solution. We conclude that there exists an optimal solution consisting of  $\lambda$  non-crossing surfaces with the minimum distance between any two adjacent surfaces no less than 1. Thus, the algorithm in Section 2.2.1 can be used to find the optimal solution.

### 3. Applications

To demonstrate the applicability of our framework, three different applications were selected. In Section 3.1, we apply our method to medical image segmentation. Section 3.2 shows our experiments on scenic image segmentation. In Section 3.3, we use our framework for image resizing.

#### 3.1. Medical Image Segmentation

In the medical imaging field, multiple objects often exist in the images, which lack clear boundaries and mutually interact each other. We employ our framework for multiple surface segmentation in the human retinal optical coherence tomography (OCT) images and for segmentation of the bladder and prostate from X-ray CT images.

##### 3.1.1 Intraretinal Layer Segmentation of OCT Images

Simultaneous segmentation of 3-D intraretinal layers is in urgent need to facilitate quantification of individual retinal layer properties [10]. The seven surfaces we desired to find are shown in Fig. 5(a) and (b). In our experiments, we used

Surface	shape prior penalty	no shape prior penalty
2	$4.90 \pm 1.02$	$5.66 \pm 1.01$
3	$6.08 \pm 1.15$	$6.97 \pm 0.98$
4	$5.59 \pm 1.04$	$7.00 \pm 0.72$
5	$5.17 \pm 0.83$	$6.04 \pm 0.91$
Overall	$5.44 \pm 1.07$	$6.42 \pm 1.05$

Table 1. Summary of the mean unsigned surface positioning errors. Mean $\pm$ SD in  $\mu m$ . Note the consistently better performance of the new method.

a similar workflow as described in [10]. Surfaces 1, 6, and 7 with relatively strong boundaries were simultaneously detected first using the graph search approach without incorporating the shape prior penalty [14]. Our new approach with the convex penalties of the shape priors was then used to simultaneously segment the remaining surfaces 2, 3, 4, and 5, which lack clear boundaries and have substantial interactions in between.

In our experiment, the gradient-based function was employed as the cost function for each voxel. To incorporate the proper shape prior information, we used the manual tracing results from the training datasets. The mean and standard deviation of how the z-value changes from column  $p$  to its neighboring column  $q$  (i.e.,  $S_i(p) - S_i(q)$ ) were learned for each surface. Let  $\bar{d}_{p,q}$  and  $\sigma_{p,q}$  denote the mean and the standard deviation of  $S_i(p) - S_i(q)$  for surface  $i$ , respectively. To allow for 99% of the shape changes from column  $p$  to column  $q$  (assuming a normal distribution), the two hard shape constraints were set as:  $\underline{\Delta}_{p,q}^i = \bar{d}_{p,q} - 2.6 \cdot \sigma_{p,q}$  and  $\bar{\Delta}_{p,q}^i = \bar{d}_{p,q} + 2.6 \cdot \sigma_{p,q}$ . For soft shape prior penalty, we employed a quadratic function,  $f_{p,q}(x) = a(x - \bar{d}_{p,q})^2$ , where  $a$  was a weighting coefficient. In our experiments, we chose  $a = 5$  according to experiments on the training sets.

For validation, 29 3-D OCT images ( $100 \times 100 \times 512$  voxels,  $12 \times 12 \times 4 \text{ mm}^3$ ) were acquired from 29 human subjects. 15 datasets were used as the training data and the remaining 14 datasets were used for performance assessment. To prove the effectiveness of our shape prior penalty, we mainly focused on segmenting surfaces 2, 3, 4, and 5. The average of the two tracings from two human experts were used as the reference standard. The unsigned surface positioning errors were computed for each surface as a shortest distance between the computed results and the reference standard.

The experiments were conducted on a Linux workstation (3 GHz, 32GB memory). The average execution time was  $10.5 \pm 2.4$  minutes for simultaneous detection of 4 surfaces. The segmentation performance is shown quantitatively in Table 1. Our method produced more accurate and smoother segmentation results compared with the previous method without the shape prior penalty [14]. For all four

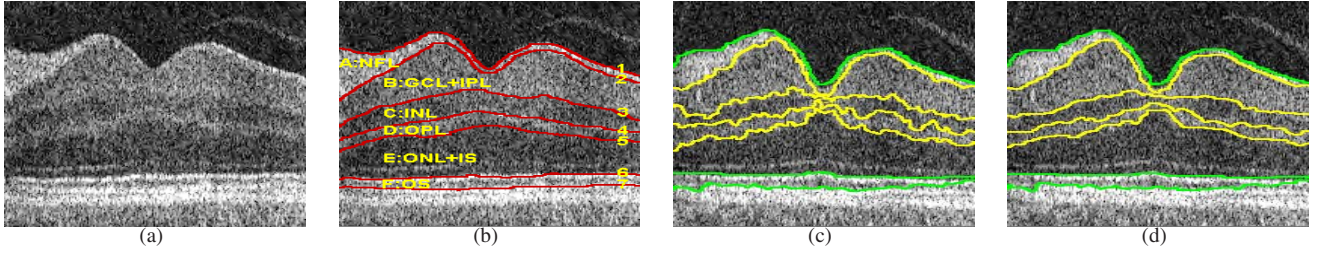


Figure 5. Intraretinal Layer Segmentation in 3-D OCT images. (a) One 2-D slice of retinal OCT. (b) Seven surfaces (labeled 1-7) and six corresponding intralayers. (c) Graph searching result shown on a 2-D slice. All 7 surfaces are found without the shape prior penalties. (d) Convex shape prior penalties are employed for surfaces 2, 3, 4, 5.

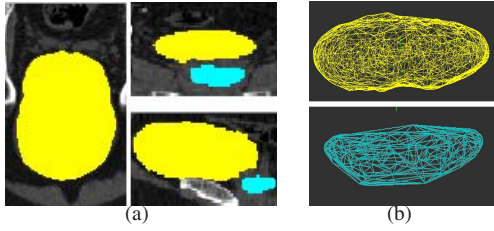


Figure 6. Bladder/prostate segmentation in 3-D CT. (a) Pre-segmentation result as the shape model for Bladder and Prostate. (b) Two meshes for bladder (yellow) and prostate (blue).

layers tested, the result shows an obvious improvement by incorporating shape prior penalties. Fig. 5(c),(d) gives the illustrative segmentation results on one 2-D slice from the 3-D volume using both methods, i.e., with and without the shape prior penalty.

### 3.1.2 Simultaneous Segmentation of Bladder and Prostate

We also tested our method on simultaneous surface detection of bladder and prostate in 3-D X-ray CT images. One main difficulty lies in the fact that the surrounding tissues of the prostate and bladder have similar intensity profiles. Thus, the incorporation of the shape prior information is necessary for an accurate segmentation.

Our method mainly consists of the following steps. First, we obtain a pre-segmentation of bladder and prostate as the initial shape model, which provides useful information about the topological structures of the target objects (Fig. 6(a)). A 3-D geodesic active contour method is employed [4] for pre-segmenting the bladder. The mean shape of the prostate from the training datasets is simply fitted to the never-before seen CT images using a rigid transform. Two meshes are built for the bladder and prostate based on the shape model (Fig. 6(b)). The graph search method with shape information is used to segment the bladder and the prostate individually. The quadratic shape prior penalty function is obtained from the experiments on the training datasets. This gives an initial segmentation for the blad-

der and the prostate boundary surfaces. However, the single surface detection does not incorporate the mutually interacting information about the bladder and prostate. The two obtained initial results may overlap each other. To resolve that problem, our multiple surface searching method with the shape prior penalty is employed to segment the bladder and the prostate simultaneously. The surface interaction constraints are incorporated to make sure that there are no overlaps between the two surfaces.

21 3-D CT images from different patients with prostate cancer were used in our experiments. The image resolution ranged from  $0.98 \times 0.98 \times 3.00 \text{ mm}^3$  to  $1.60 \times 1.60 \times 3.00 \text{ mm}^3$ . 8 datasets were randomly selected as the training datasets to build the shape model. Our experiments were carried out on the remaining 13 datasets. The segmentation results were compared with the expert-defined independent standard. For quantitative validation, the unsigned surface positioning errors were computed for the bladder and the prostate surfaces as minimal distances between the computed result and the manual contour.

The experiments were conducted on a WinXP PC (2.13GHz, 2GB memory). The average execution time for graph search was  $32.5 \pm 4.2$  seconds for CT image sizes ranging from  $80 \times 120 \times 30$  to  $190 \times 180 \times 80$  voxels. All 13 datasets were successfully segmented. The output results agreed with the manual contours quite well, especially considering the difficulty of the segmentation in the pelvic region. The overall mean unsigned surface positioning errors were  $1.04 \pm 0.15 \text{ mm}^3$  ( $0.78 \pm 0.11$  voxel) for the bladder and  $1.09 \pm 0.19 \text{ mm}^3$  ( $0.82 \pm 0.13$  voxel) for the prostate. Fig. 7(a) shows one segmentation result in three orthogonal views. Fig. 7(b) is the 3-D representation of the segmentation result.

### 3.2. Scenic Image Segmentation

Our new method was also applied to the scenic image segmentation. Fig. 8(a) shows the segmentation obtained without the prior shape penalty term. The result was affected by the distracting vertical textures. In Fig. 8(b), a shape prior penalty was incorporated, which penalized the

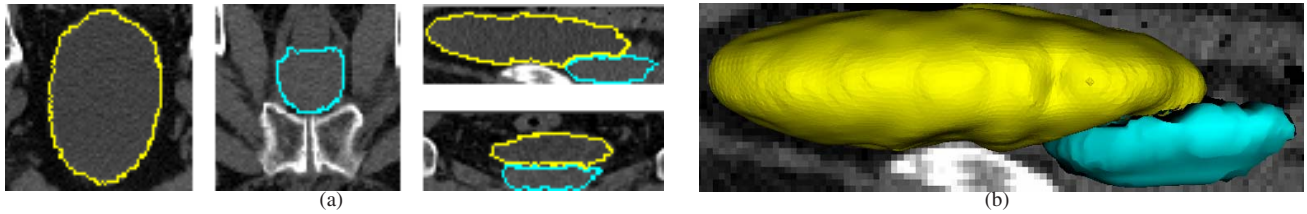


Figure 7. Segmentation result of the bladder (yellow) and the prostate (blue). (a) Three orthogonal views of the segmentation (transverse, sagittal, coronal). (b) 3-D rendering of the segmentation result.

shape changes in the vertical direction. Fig. 8(c) shows the result for the inner and outer borders of the sunflower using the shape prior control. For the inner border, we used the penalty function favoring a circular shape. The outer border expresses frequent zigzags. Thus, a large hard shape constraint and a small shape prior penalty were used to allow a more flexible border.

### 3.3. Image Resizing

In recent years, there has been increasing interest in image resizing due to its relevance to image display on devices with different resolutions [1, 11]. Our main idea for image resizing is similar to that used in [11]. The image resizing problem is formulated as an optimization problem, which seeks multiple surfaces whose total energy is minimized. By removing or inserting those surfaces, content-aware image resizing is achieved.

The framework reported in [11] only used the node-weighted graph representation without incorporating shape prior penalties, which may cause artifacts due to the discontinuity between the neighboring columns. Here we use our algorithm in Section 2 to resolve that problem. The shape prior penalty is incorporated to penalize the shape change between the neighboring columns. Note that in the image resizing problem, the sought surfaces may cross each other, but share no common voxels. As proved in Section 2.2, if we apply the same cost functions and the same shape prior functions to all surfaces – which is reasonable in the image resizing problem, this problem can be transformed into the problem of finding an optimal solution for detecting multiple non-crossing surfaces. The minimum distance between any two adjacent surface is no less than 1. Thus the algorithm in Section 2.2.1 is applicable for solving this problem.

Fig. 9 shows our result on four 2-D images. Improvements indicated by arrows can be appreciated from the incorporation of the shape prior penalty.

## 4. Conclusion

We have reported an algorithm for multiple surface detection incorporating a shape prior term using convex pairwise energies. A globally optimal solution is obtained by computing a maximum flow in low-order polynomial time.

Compared with other graph-based methods, our approach provides more local and more flexible control. We have also reported an algorithm for detecting multiple crossing surfaces with no shared voxels. Our methods were applied to solving several application problems, including medical image segmentation, scenic image segmentation, and image resizing. All produced high quality results.

**Acknowledgments** This research was supported in part by the NSF grants CCF-0830402 and CCF-0844765, and the NIH grants R01 EB004640 and K25 CA123112.

## References

- [1] S. Avidan and A. Shamir. Seam carving for content-aware image resizing. *ACM Transactions on Graphics*, 26(3), 2007.
- [2] Y. Boykov and G. Funka-Lea. Graph cuts and efficient N-D image segmentation. *Int. Journal of Computer Vision*, 70(2):109–131, 2006.
- [3] Y. Boykov, O. Veksler, and R. Zabih. Fast approximate energy minimization via graph cuts. *IEEE Trans. Pattern Anal. Machine Intell*, 23(11):1222–1239, 2001.
- [4] V. Caselles, R. Kimmel, and G. Sapiro. Geodesic active contours. *International journal on computer vision*, 22:61–97, 1997.
- [5] A. Delong and Y. Boykov. Globally optimal segmentation of multi-region objects. In *Proc. IEEE International Conference on Computer Vision*, 2009.
- [6] X. Dou, X. Wu, A. Wahle, and M. Sonka. Globally optimal surface segmentation using regional properties of segmented objects. In *Proc. IEEE International Conference on Computer Vision and Pattern Recognition*, pages 1–8, 2008.
- [7] P. Felzenszwalb. Representation and detection of deformable shapes. *IEEE Trans. Pattern Anal. Machine Intell*, 27(2):208–220, 2005.
- [8] D. Freedman and T. Zhang. Interactive graph cut based segmentation with shape priors. In *Proc. IEEE International Conference on Computer Vision and Pattern Recognition*, volume 1, pages 755–762, 2005.
- [9] L. Grady. Computing exact discrete minimal surfaces: extending and solving the shortest path problem in 3D with application to segmentation. In *Proc. IEEE International Conference on Computer Vision and Pattern Recognition*, volume 1, pages 69–78, 2006.
- [10] M. Haeker, M. Abramoff, X. Wu, S. Russell, T. Burns, and M. Sonka. Automated 3-D intraretinal layer segmentation



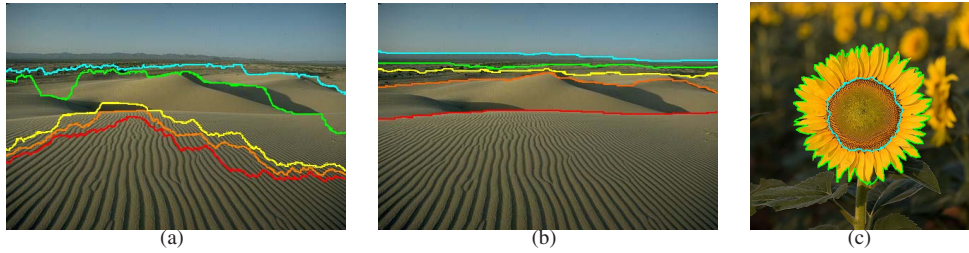


Figure 8. Scenic Image Segmentation. (a) Segmentation performed without the shape prior penalty. (b) Penalizing the shape changes in the vertical direction. (c) Segmenting the sunflower boundaries with the shape prior control. For the inner border (blue), our shape prior function favored a circular shape. For the outer border (green), a small shape prior penalty was incorporated to allow a more flexible border.



Figure 9. Image resizing using graph search method. The first row is the original image. The second row is the graph search result without the shape prior penalty. The third row is the result with the convex shape prior penalties. Typical improvements are pointed out by arrows.

- of macular spectral-domain optical coherence tomography images. *IEEE Trans. Medical Imaging*, 28(9):1436–1447, 2009.
- [11] D. Han, X. Wu, and M. Sonka. Optimal multiple surfaces searching for video/image resizing - a graph-theoretic approach. In *Proc. IEEE International Conference on Computer Vision*, 2009.
- [12] H. Ishikawa. Exact optimization for markov random fields with convex priors. *IEEE Trans. Pattern Anal. Machine Intell.*, 25(10):1333–1336, 2003.
- [13] K. Li and M. Jolly. Simultaneous detection of multiple elastic surfaces with application to tumor segmentation in CT images. In *Proc. SPIE Medical Imaging: Image Processing*, volume 6914, 2008.
- [14] K. Li, X. Wu, D. Chen, and M. Sonka. Optimal surface segmentation in volumetric images - a graph-theoretic approach. *IEEE Trans. Pattern Anal. Machine Intell.*, 28(1):119–134, 2006.
- [15] J. Malcolm, Y. Rathi, and A. Tannenbaum. Graph cut segmentation with nonlinear shape priors. In *Proc. IEEE International Conference on Image Processing*, 2007.
- [16] T. Schoenemann and D. Cremers. Globally optimal image segmentation with an elastic shape prior. In *Proc. IEEE International Conference on Computer Vision*, 2007.
- [17] Q. Song, X. Wu, Y. Liu, M. Smith, J. Buatti, and M. Sonka. Optimal graph search segmentation using arc-weighted graph for simultaneous surface detection of bladder and prostate. In *Proc. International Conference on Medical Image Computing and Computer-Assisted Intervention*, pages 827–835, 2009.
- [18] N. Vu and B. Manjunath. Shape prior segmentation of multiple objects with graph cuts. In *Proc. IEEE International Conference on Computer Vision and Pattern Recognition*, Jun 2008.
- [19] X. Wu and D. Chen. Optimal net surface problems with applications. In *Proc. 29th International Colloquium on Automata, Languages and Programming*, pages 1029–1042, 2002.